

Numerical study of hyperlenses for three-dimensional imaging and lithography

Weiwei Wan,¹ Joseph Louis Ponsetto,¹ and Zhaowei Liu*

Department of Electrical and Computer Engineering, University of California, San Diego, California 92093, USA

¹These authors contributed equally

*zhaowei@ucsd.edu

Abstract: The development of nanostructured metamaterials and the ability to engineer material dispersion has led to impressive advances in the diverse field of nanophotonics. Of interest to many is the enhanced ability to control, illuminate, and image with light on subwavelength scales. In this letter, we numerically demonstrate a hyperlens with unprecedented radial-resolution at 5 nm scale for both imaging and lithography applications. Both processes are shown to have accuracy that surpasses the Abbe diffraction limit in the radial direction, which has potential applications for 3D imaging and lithography. Design optimization is discussed with regards to several important hyperlens parameters.

©2015 Optical Society of America

OCIS codes: (160.1190) Anisotropic optical materials; (160.3918) Metamaterials; (220.3630) Lenses.

References and links

1. M. Born and E. Wolf, *Principles of Optics* (Cambridge University Press, 1999).
2. B. Hecht, B. Sick, U. P. Wild, V. Deckert, R. Zenobi, O. J. F. Martin, and D. W. Pohl, "Scanning near-field optical microscopy with aperture probes: fundamentals and applications," *J. Chem. Phys.* **112**(18), 7761–7774 (2000).
3. M. J. Rust, M. Bates, and X. Zhuang, "Sub-diffraction-limit imaging by stochastic optical reconstruction microscopy (STORM)," *Nat. Methods* **3**(10), 793–796 (2006).
4. E. Betzig, G. H. Patterson, R. Sougrat, O. W. Lindwasser, S. Olenych, J. S. Bonifacino, M. W. Davidson, J. Lippincott-Schwartz, and H. F. Hess, "Imaging intracellular fluorescent proteins at nanometer resolution," *Science* **313**(5793), 1642–1645 (2006).
5. M. G. Gustafsson, "Nonlinear structured-illumination microscopy: wide-field fluorescence imaging with theoretically unlimited resolution," *Proc. Natl. Acad. Sci. U.S.A.* **102**(37), 13081–13086 (2005).
6. V. G. Veselago, "The electrodynamics of substances with simultaneously negative values of ϵ and μ ," *Sov. Phys. Usp.* **10**, 509–514 (1968).
7. J. B. Pendry, "Negative refraction makes a perfect lens," *Phys. Rev. Lett.* **85**(18), 3966–3969 (2000).
8. J. Pendry, "Perfect cylindrical lenses," *Opt. Express* **11**(7), 755–760 (2003).
9. N. Fang, H. Lee, C. Sun, and X. Zhang, "Sub-diffraction-limited optical imaging with a silver superlens," *Science* **308**(5721), 534–537 (2005).
10. A. Salandrino and N. Engheta, "Far-field subdiffraction optical microscopy using metamaterial crystals: theory and simulations," *Phys. Rev. B* **74**(7), 075103 (2006).
11. Z. Jacob, L. V. Alekseyev, and E. Narimanov, "Optical hyperlens: far-field imaging beyond the diffraction limit," *Opt. Express* **14**(18), 8247–8256 (2006).
12. Z. Liu, H. Lee, Y. Xiong, C. Sun, and X. Zhang, "Far-field optical hyperlens magnifying sub-diffraction-limited objects," *Science* **315**(5819), 1686 (2007).
13. H. Lee, Z. Liu, Y. Xiong, C. Sun, and X. Zhang, "Development of optical hyperlens for imaging below the diffraction limit," *Opt. Express* **15**(24), 15886–15891 (2007).
14. G. Lerosey, J. de Rosny, A. Tourin, and M. Fink, "Focusing beyond the diffraction limit with far-field time reversal," *Science* **315**(5815), 1120–1122 (2007).
15. G. Bartal, G. Lerosey, and X. Zhang, "Subwavelength dynamic focusing in plasmonic nanostructures using time reversal," *Phys. Rev. B* **79**(20), 201103 (2009).
16. Y. Xiong, Z. Liu, and X. Zhang, "A simple design of flat hyperlens for lithography and imaging with half-pitch resolution down to 20 nm," *Appl. Phys. Lett.* **94**(20), 203108 (2009).
17. L. Chen and G. P. Wang, "Pyramid-shaped hyperlenses for three-dimensional subdiffraction optical imaging," *Opt. Express* **17**(5), 3903–3912 (2009).

18. J. Rho, Z. Ye, Y. Xiong, X. Yin, Z. Liu, H. Choi, G. Bartal, and X. Zhang, "Spherical hyperlens for two-dimensional sub-diffractive imaging at visible frequencies," *Nat. Commun.* **1**(9), 143–147 (2010).
19. P. B. Johnson and R. W. Christy, "Optical constants of the noble metals," *Phys. Rev. B* **6**(12), 4370–4379 (1972).
20. Q. Meng, X. Zhang, L. Cheng, P. Cao, Y. Li, H. Zhang, and G. Wang, "Deep subwavelength focusing of light by a trumpet hyperlens," *J. Opt.* **13**(7), 075102 (2011).
21. S. A. Cummer, B.-I. Popa, D. Schurig, D. R. Smith, and J. Pendry, "Full-wave simulations of electromagnetic cloaking structures," *Phys. Rev. E Stat. Nonlin. Soft Matter Phys.* **74**(3), 036621 (2006).
22. Z. Jacob, L. V. Alekseyev, and E. Narimanov, "Semiclassical theory of the hyperlens," *J. Opt. Soc. Am. A* **24**(10), A52–A59 (2007).
23. E. D. Palik, *Handbook of Optical Constants of Solids* (Academic Press, 1998).
24. A. P. Zhang, X. Qu, P. Soman, K. C. Hribar, J. W. Lee, S. Chen, and S. He, "Rapid fabrication of complex 3D extracellular microenvironments by dynamic optical projection stereolithography," *Adv. Mater.* **24**(31), 4266–4270 (2012).
25. C. Ma, R. Aguineldo, and Z. Liu, "Advances in the hyperlens," *Chin. Sci. Bull.* **55**(24), 2618–2624 (2010).
26. D. Lu and Z. Liu, "Hyperlenses and metalenses for far-field super-resolution imaging," *Nat. Commun.* **3**, 1205–1213 (2012).

1. Introduction

The optical microscope has been enabling important scientific discoveries since its invention centuries ago. The ability to observe features and processes otherwise invisible to the human eye has broadened the scope of scientific knowledge considerably, especially in life sciences and microelectronics. The resolution of a standard microscope is limited, however, by the Abbe diffraction limit [1] to approximately 200 nm for visible light wavelengths. To observe elusive sub-diffraction features, various approaches are used such as near-field scanning optical microscopy (NSOM) [2], stochastic optical reconstruction microscopy (STORM) [3], photoactivated localization microscopy (PALM) [4] and saturated structured illumination microscopy (SSIM) [5]. However, most of these methods involve high-intensity light or slow scanning processes, which limits usefulness for imaging sensitive, dynamic biological samples.

With the realization and exploitation of negative index materials [6], many new imaging tools have been developed at optical frequencies. The perfect lens [7] was proposed to aid in high-resolution imaging by allowing detection of larger wavevectors, which ordinarily are lost to evanescent decay. In recent years, many variations of the perfect lens idea have been proposed and demonstrated, including the cylindrical perfect lens [8], the superlens [9], but these all rely on near-field imaging techniques.

As fabrication abilities have improved, thin metal-dielectric multilayer structures possessing hyperbolic dispersion relations have emerged as a way to capture evanescent details in the far-field. These structures, when used for imaging, are known as hyperlenses [10–13]. A hyperlens is comprised of alternating metal and dielectric planar layers with deeply sub-wavelength thicknesses.

Because of the aforementioned dispersion relation, large wavevectors that decay exponentially in free space may propagate along the radial (ρ) direction in a hyperlens. Additionally, by curving the overall multilayer into concentric structure, a magnifying effect is obtained, which gradually shrinks the spatial frequency components as they reach layers with larger radii. By careful design, this can transform high-spatial-frequency information into the collectable aperture of an otherwise standard optical system. This is the primary function of the hyperlens as an imaging apparatus.

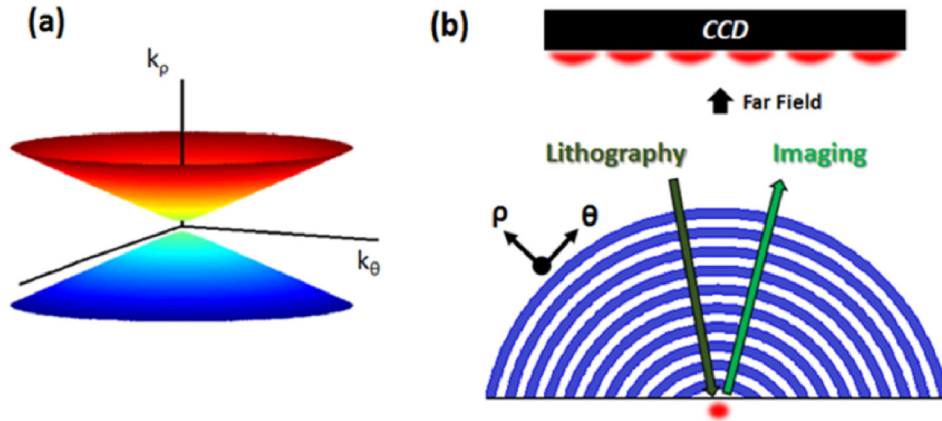


Fig. 1. (a) Isofrequency surface in a hyperbolic metamaterial with $\epsilon_\rho < 0$ and $\epsilon_\theta > 0$. (b) Illustration of a hyperlens structure, showing the time reversal concept. If a point source imaged by a hyperlens produces a given wavefront at the CCD plane, then the same distribution (accounting for losses) sent in the opposite direction will focus to a point on the other side of the hyperlens.

The concept of time reversal in electromagnetic [14, 15] allows us to think of the hyperlens as having two potential applications for both imaging and lithography [16], as illustrated schematically in Fig. 1(b). In one direction, high spatial frequencies from a source are converted to propagating light and collected at a detector such as a charge-coupled device (CCD). This is the imaging configuration. In the opposite direction, a specially-designed diffraction-limited wavefront can be sent into the hyperlens and have its features spatially compressed, resulting in a sub-wavelength focus point for use in lithography.

In past work on hyperlenses, super resolution has been primarily discussed only in the lateral direction. Pyramid-shaped hyperlenses have been designed [17] with a specialized geometry that enables some limited sub-diffraction imaging of sources distributed in three dimensions. However, with this method, there is no clear way to discern the z -position of an object without a priori knowledge. In our paper, we look carefully at the radial resolution of a spherical multilayer hyperlens. The dispersion and geometry of this design allows for far-field focusing behavior that is highly sensitive to radial position. We show the ability to resolve differences in radial position as small as 5 nm, in concert with lateral super resolution, via simple far-field detection.

Any significant z separation between an object and the hyperlens surface has, to date, been regarded as sub-optimal, since the evanescent field strength drops off exponentially away from the object. However, within a thin volume close to the surface, evanescent fields from objects with a distribution of z depths can be focused and imaged in the far-field. This allows for three dimensional super resolution imaging and lithography.

2. Hyperlenses for imaging in the radial direction

To examine the imaging capability of a hyperlens in the radial direction, two-dimensional full-wave simulations using COMSOL Multiphysics were conducted. The polarization-dependent behavior of the hyperlens dictates that only the transverse magnetic (TM) field components will propagate and contribute to a resolved image. Transverse electric (TE) components will be reflected and will neither contribute to nor degrade the hyperlens performance [18]. A TM-polarized point source was placed several nanometers away from the hyperlens surface, and the propagation through the hyperlens and out on the other side was monitored. For the most realistic result, a real multilayer structure was used in our model. The metal layer material used was silver ($\epsilon_m = -2.4 - 0.25i$). The dielectric layers had

permittivity $\epsilon_d = 3.75$, and the imaging half space had a permittivity of 3.217. The real permittivity in the vicinity of the point sources was chosen as 2.89. The real silver permittivity for 365 nm light was based on an interpolation of previous experimental measurements [19]. The metal filling fraction p was 0.5. For these calculations, the radii of the inner and outer hyperlens layers were 400 nm and 1840 nm, respectively. Numerical calculation time was shortened by restricting the simulated region to a central area where the vast majority of the field strength was concentrated. This restriction is acceptable because the anisotropic nature of the hyperlens medium prevents significant propagation in the tangential direction. Perfectly matched layer boundaries were added at the top and bottom of the simulation region to reduce unwanted reflections. Results are shown in Fig. 2.

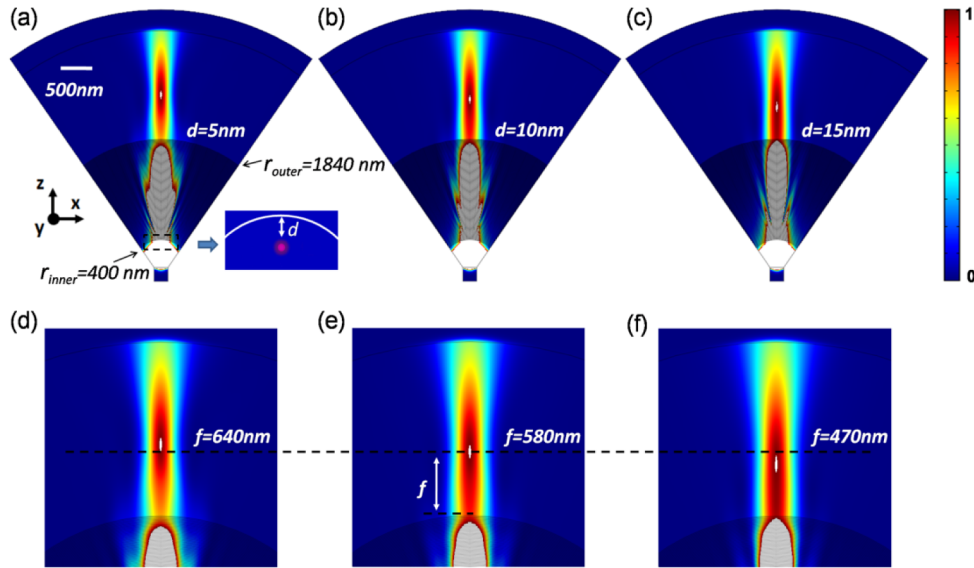


Fig. 2. (a)-(c) Intensity distributions for imaging of a point source at varying separations d (5, 10, 15 nm) from the inner hyperlens surface. The radii of the inner and outer hyperlens layers were 400 nm and 1840 nm, respectively. The thickness of each layer is 10 nm. The colorbar represents the normalized, linear-scale intensity. Note that the white areas indicate “saturated” intensity above the normalization value, which was chosen for illustrative purposes to show the focus spot clearly. (d)-(f) A closer look at the intensity focus spot movement in (a)-(c). The focal positions away from the outermost surface [f] are 640, 580, 470 nm, respectively. The white size bar in (a) indicates 500 nm.

The radial separation of the point source from the hyperlens surface was set to $d = 5, 10$ and 15 nm. In all cases, the emitted light captured by the hyperlens was refocused to a point f (defined along the radial direction) away from the outermost surface of the hyperlens, which was defined as $f = 0$. Note that the results for each of the three separations were contrasted to clearly show the focus point. For separations of 5, 10 and 15 nm, the focus position was at $f = 640, 580$ and 470 nm, respectively. We see that the focus point position f varies significantly when d is changed.

As light travels through the hyperlens, the lateral k -vectors from the object are compressed and the resulting image is projected into the far-field. The change in f with respect to the change in d is also magnified, nearly by a factor of 17. This has potential to bring very fine depth resolution into a far-field measurement. In Fig. 2(b), we see a close look at the focus spot movement as a function of d . For only a ten nanometer change in d , we have more than 150 nm change in f , which can be detected quite easily using mechanical translation stages.

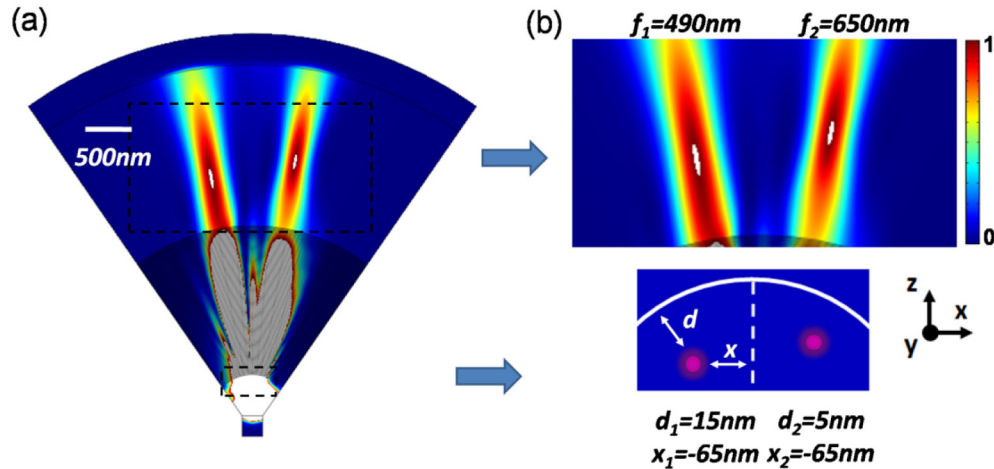


Fig. 3. (a) Imaging result for two 365 nm sources, showing focusing at two different positions for the two sources. The white size bar indicates 500 nm. (b) Magnified view of the focus spots and a schematic illustration of the source positions. The two point sources are 130 nm apart in x , and just 10 nm apart in the radial [ρ] direction. The far-field foci differ by 160 nm in ρ .

Figure 3(a) shows the simultaneous focusing result for two point sources. As pictured in Fig. 3(b), although the sources are 130 nm apart in x , and just 10 nm apart in ρ , their far-field focus points are dramatically separated on the other side of the hyperlens (160 nm apart in ρ and even further separated in x). Because the light is steered along in the ρ direction within the hyperlens, the small initial separation is magnified considerably.

The hyperlens is well known to have sub-diffraction imaging capability in the lateral direction. We have shown here that in addition, extremely fine radial resolution can be achieved. This is a coveted capability for imaging of biological specimens. By stepping a motorized z -stage, or potentially by recording in multiple z -planes simultaneously, a three-dimensional image can be obtained, although the total image depth in z direction is always limited by the evanescent wave decay length.

3. Hyperlens theory and design

Many geometrical variations of the multilayer hyperlens [16, 20] have been explored for the overall shape of the multilayer structure, ranging from flat to spherical to trumpet shapes. For shaping and focusing wavefronts in the manner of a lens, a broad spatial curvature is favored.

Analysis based on effective medium theory (EMT) [13] of a subwavelength, anisotropic multilayer structure such as a hyperlens reveals a hyperbolic dispersion relation, as shown in Fig. 1(a) and described as,

$$\frac{k_\theta^2}{\epsilon_\rho^2} + \frac{k_\rho^2}{\epsilon_\theta^2} = \frac{\omega^2}{c^2} \quad (1)$$

Where k_θ and k_ρ represent the wave-vector components in orthogonal directions, ω is the angular frequency, and c is the speed of light. ϵ_ρ is the permittivity in the ρ direction, while ϵ_θ is the permittivity in the θ plane, which is parallel to the layer orientation as shown in Fig. 1(b). The permittivities are defined as

$$\begin{aligned}\varepsilon_\theta &= p\varepsilon_m + (1-p)\varepsilon_d \\ \varepsilon_\rho &= \frac{\varepsilon_m\varepsilon_d}{(1-p)\varepsilon_m + p\varepsilon_d}\end{aligned}\quad (2)$$

where ε_m and ε_d are the frequency-dependent permittivities of the metal and dielectric materials used in the multilayer. p represents the filling fraction of metal in the structure. If Cartesian coordinates are needed, the effective permittivity ($\varepsilon_{xx}, \varepsilon_{xy}, \varepsilon_{yy}$) of a hyperlens can be calculated according to [21]. A multilayer hyperlens has negative permittivity in the ρ direction, and positive permittivity in the θ plane.

Choice of multilayer materials is an important step in the design process of the hyperlens. The conductive layer must support surface plasmon polaritons excitable by the illuminating light. In our case, using silver enabled operation towards the short-wavelength end of the visible spectrum, which is commonly used for both imaging and lithography purposes. Another key “lever” we can pull in our design process is the material we choose as our dielectric spacing layer. The desirable material properties should be low loss and a permittivity and refractive index that yield an effective medium with the desired dispersion relation.

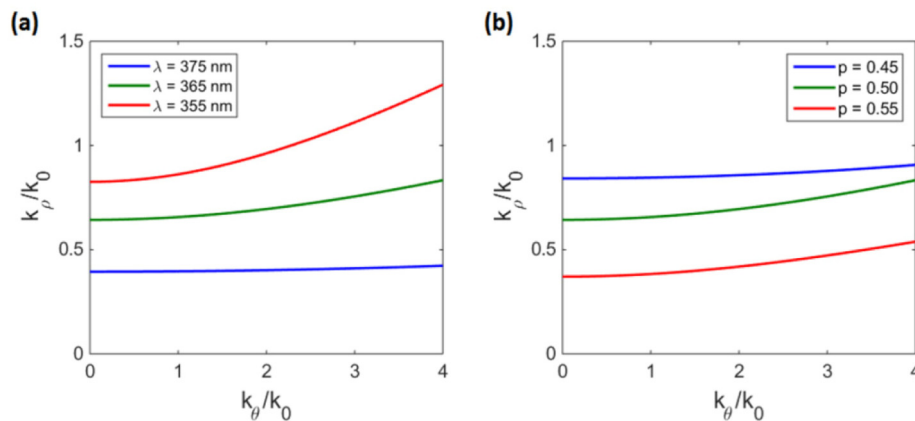


Fig. 4. Analytically calculated isofrequency curves for different (a) wavelengths with a fixed metal filling factor [$p = 0.5$] and (b) filling factors with a fixed operational wavelength [$\lambda = 365$ nm] in various hyperlens designs.

In fact, the nature of the hyperbolic dispersion curve can be fairly sensitive to a number of parameters. Shown in Figs. 4(a) and 4(b) is a series of isofrequency curves for a hyperlens with a single variable changed. It bears mentioning that at the operating frequency, a desirable dispersion curve should be broad and flat. When the slope is steeper, the wave will experience higher loss and the Poynting vector will be directed at an angle relative to the multilayer ρ axis.

A design parameter that should be delicately tuned in a hyperlens is the metal filling fraction. The relative percentage of metallic and dielectric materials has a strong effect on the material behavior. Dependent on each layer thickness, fabrication limits may also come into consideration. Physically, the dispersion relation will have a direct influence on the focusing and imaging performance of the hyperlens. The group velocity of propagating light in a medium is equal to the slope $d\omega/dk$, and the phase velocity is equal to the ratio ω/k . These two terms will dictate the phase, amplitude, and directionality of light passing through the hyperlens.

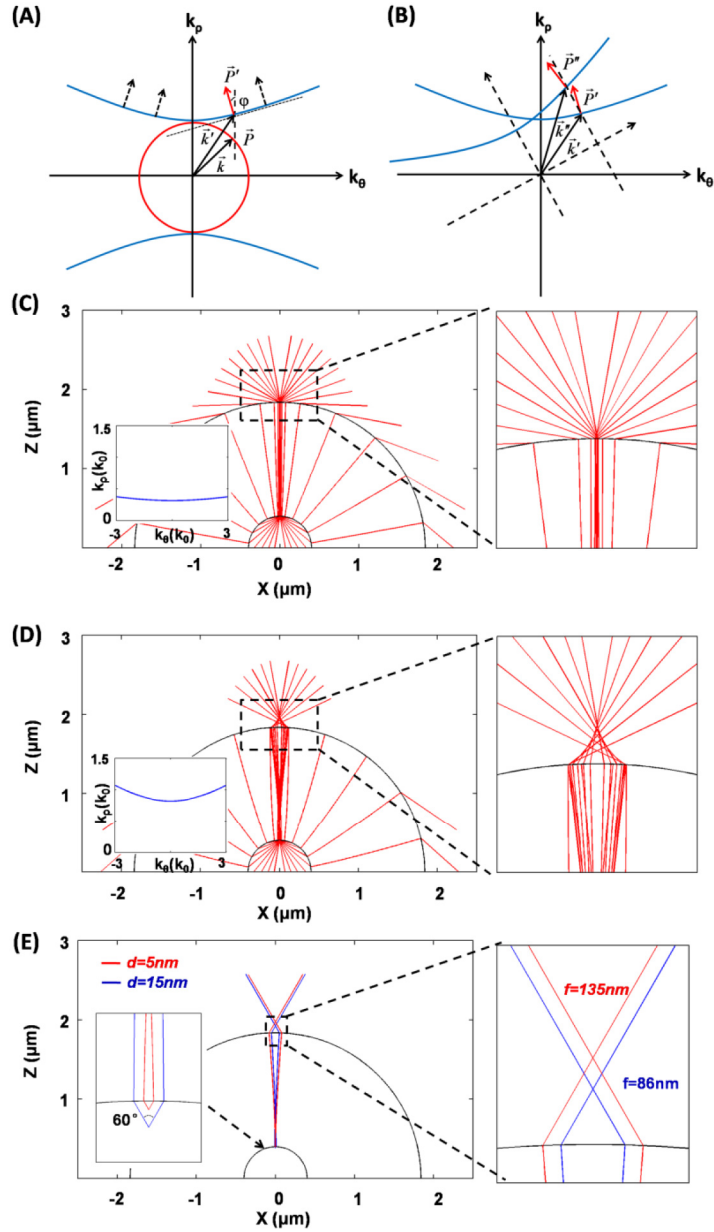


Fig. 5. The hyperlens has a local dispersion based on the wavevector components in the θ and ρ directions for a ray entering and propagating within a hyperlens. (a) Poynting vector \vec{P}' and wavevector \vec{k}' for a ray entering a hyperlens (blue isofrequency curve) from a vacuum (red isofrequency curve). (b) \vec{P}'' and \vec{k}'' for a ray propagating within a hyperlens. Changes from \vec{P}' and \vec{k}' at the initial surface of the hyperlens are a result of the ray's changing orientation relative to the layer geometry during propagation. (c) and (d) show the ray tracing calculation for $\epsilon_d = 2.6$ and $\epsilon_d = 3.75$, respectively. The corresponding dispersions are shown in the inset. The radii of the inner and outer hyperlens layers were 400 nm and 1840 nm, respectively. The separation between the point source and the inner surface is set to $d = 5$ nm.

(e) Ray tracing diagram illustrating the focusing behavior for different object positions with $\epsilon_d = 3.75$. Only one pair of incident rays with equal angle is shown.

Based on a simplified ray-tracing analysis [22], we can further analyze the design and functionality of the hyperlens. The Poynting vector \vec{P} represents the directional electromagnetic energy flux density, and also gives us the directionality of a ray in a ray-tracing picture. In a low-loss scenario, the Poynting vector always points in a perpendicular direction to the isofrequency curve. Thus, in hyperbolic materials, \vec{P} and \vec{k} are usually not in parallel. Note that due to conservation of momentum, the wavevector component parallel to an interface is always conserved. Thus, if we know the initial k_θ , we can quickly calculate the angle φ that the Poynting vector makes with the $\hat{\rho}$ axis, starting from Eq. (1).

$$\tan \varphi = \frac{\partial k_\rho}{\partial k_\theta} = \frac{\epsilon_\theta k_\theta}{\epsilon_\rho k_\rho} = \frac{\epsilon_\theta}{\epsilon_\rho} \frac{k_\theta}{\sqrt{\epsilon_\theta (k_0^2 + \frac{k_\theta^2}{\epsilon_\rho})}} \quad (3)$$

Figure 5(a) illustrates the group velocity (in the Poynting vector \vec{P}' direction) and phase velocity (in the wavevector \vec{k}' direction) for a ray entering a hyperlens from a vacuum with initial wavevector \vec{k} . Note that the Poynting vector is parallel to \vec{k} in the vacuum. Because the hyperlens has a curved multilayer geometry, rays with an initial incident angle will see changes in the local dispersion as they propagate inside of a hyperlens, since their orientation relative to the local coordinates will also be changing. This will affect the Poynting vector and the wavevector during propagation between the layers in a hyperlens, as shown in Fig. 5(b). The result from a ray-tracing perspective is a subtle bending of the ray path.

In Fig. 5(c) and 5(d), we show how this ray tracing approach can be used to design the dispersion property of a hyperlens in order to optimize the material properties in our full wave simulations. Here, d is set to 5 nm, and $p = 0.5$. As an example, we change only one parameter, the permittivity of the dielectric layers. The result of this change is a change in the dispersion relation, which directly affects the ray tracing path. For $\epsilon_d = 2.6$, the isofrequency curve is quite flat. The light propagates almost completely along radial direction and forms a focal image at the outer interface. For $\epsilon_d = 3.75$, we see a greater curvature in the dispersion, and a greater bending of the light. The rays are successfully focused at a point away from the outer surface of the hyperlens. It should be noted that the results in Fig. 5 are shown as a conceptual illustration; phase is not considered in this simplified model. We can clearly see that by altering the permittivity of the dielectric layers, we can dramatically change the focusing location of the hyperlens.

Interestingly in our imaging simulations, the focal position f gets closer to the hyperlens as the source position d gets farther away. We also calculated the path of a few rays with 30° off-axis angles, generating Fig. 5(e) for different source positions (5 nm and 15 nm). We note that the rays undergo a subtle bending as they travel through the hyperlens, a behavior which is dependent on the initial k_θ . We can see very clearly that the separation of the point source from the initial surface of the hyperlens will directly affect the focusing distance on the outer side. Matching with our COMSOL simulations, there is an inverse relationship observed between d and f .

4. Hyperlenses for lithography in the radial direction

For an exploration of deeply sub-wavelength focusing with potential for application in lithography, simulations of a real hyperlens multilayer structure were conducted. Shown in Fig. 6(a) is the full wave simulation result and the real multilayer modeled geometry of the hyperlens. The inner surface of the hyperlens is assumed to be polished flat in this

calculation. Alternating layers of silver ($\epsilon_{Ag} = -2.4-0.25i$) and Al_2O_3 ($\epsilon_{\text{Al}_2\text{O}_3} = 3.217$) were used, with realistic material parameters [19, 23]. Each layer was 10 nm thick. The outermost layer had a radius of curvature of 1400 nm, and the innermost layer had a radius of curvature of 600 nm. The illumination wavelength was chosen to be 365 nm, as this is an important wavelength in lithography applications.

Our time-reversal strategy involved two main steps. First, we calculated the far-fields detected through a hyperlens from a point source placed in the location we wish to use for lithography. The simplest design possesses a single spot below the center of the flat edge of the lens. Second, knowing the loss properties and geometry of the hyperlens, we can design a specific wavefront to send in the reverse direction to recreate the point source, or at least as small a spot as the hyperlens can manage. Because light propagates in the opposite direction, the spatial frequencies of the incoming wavefront are in fact increased dramatically, and so an otherwise unattainable sub-wavelength focus for lithography is realized.

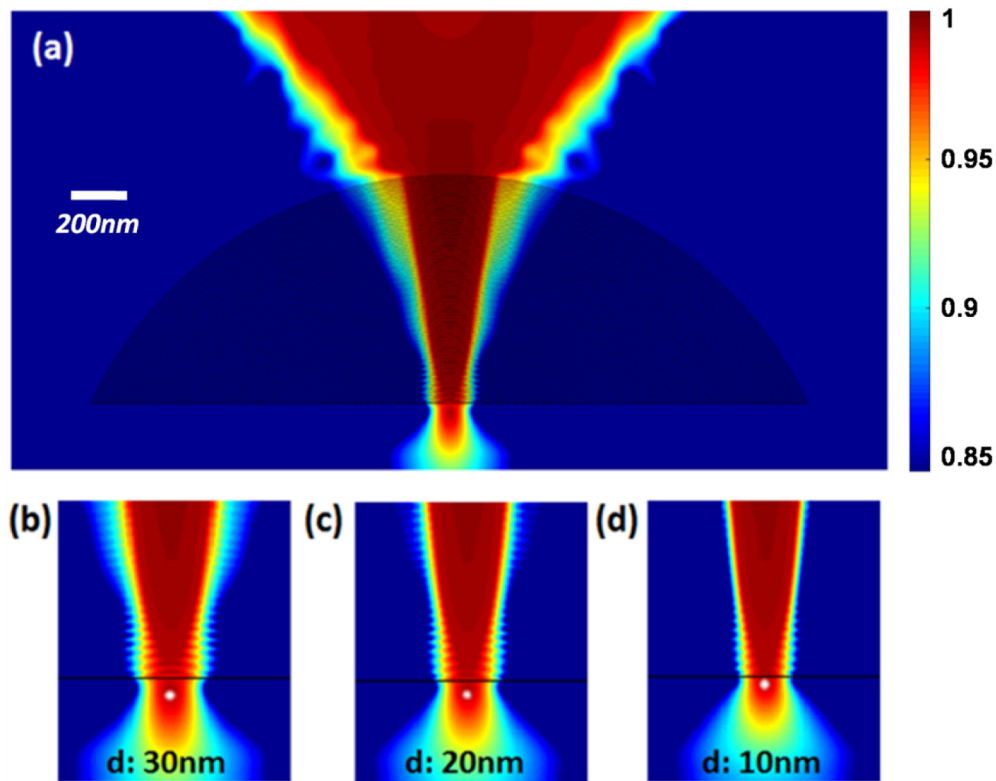


Fig. 6. (a) Multilayer structure for focusing ultraviolet light to a point using a hyperlens. The radii of the inner and outer hyperlens layers were 600nm and 1400nm, respectively. The normalized log-scale intensity is shown. The scale bar represents 200 nm. (b), (c), (d) Different distributions of amplitude and phase in three wavefronts sent towards the curved surface of the hyperlens result in three different focal z -depths. Note that d represents the spacing of the local maxima away from the hyperlens surface. This shows potential for very fine control of three-dimensional lithographic patterns. Note that the local maxima are highlighted with white color.

Optical fabrication via stereolithography has many promising applications including creation of complex 3D extracellular microenvironments [24]. An extremely fine z -resolution was numerically demonstrated above for imaging. We can also achieve a similarly deep sub-wavelength z control in lithography, as shown in Figs. 6(b)-6(d). By calculating the necessary wavefronts for different lithographic focus point positions, we can control the depth precisely.

Because the hyperlens increases the k_θ component of light propagating in the radial direction, the focus spot will be tighter in all three dimensions than what would normally be achievable in a diffraction-limited setup.

The x - y resolution ability of the hyperlens is well established [25, 26]. In combination with the z performance shown in this work, we now can see the potential for three-dimensional super resolution imaging and lithography capability.

5. Conclusion and discussion

We numerically demonstrate the super radial-resolution capability of hyperlenses, which has potential applications for 3D imaging and lithography within a thin volume close to the inner surface. Applications where visible-light super resolution is desired in conjunction with three dimensional capabilities are most obvious in biological fields. Since many sub-cellular and intracellular processes occur on the millisecond time scale, having high-speed potential is also attractive. Three-dimensional lithography and more generally scanning of a fine point of light with precise control could aid in a wide variety of patterning and manipulation tools.

There are some practical issues to be confronted with any multilayer hyperlens. Since the super resolution mechanism relies on the collection of evanescent fields, the sample of interest must be placed very close to the hyperlens. For objects thicker than several tens of nanometers, the evanescent decay will quickly become problematic. Despite this depth limitation, it should be feasible to fabricate (via lithography) or image larger 3D volumes using a layer-by-layer approach, similar to what is done in stereolithography [24] and 3D printing. With this approach, the final 3D structure height would be the individual layer depth multiplied by the number of layers. However, for certain applications, the combination of three-dimensional control and a strictly enforced and shallow z -range can be useful for eliminating unwanted background signal. These results hold promise for the development of hyperlenses with impressive 3D super resolution performance which avoid the typical sacrifices in speed and biological compatibility. Experimental implementation can be achieved without introducing prohibitive cost or complexity. As fabrication abilities continue to improve, new geometries and new possibilities will emerge. The 3D super resolution capability of the hyperlens shows great promise for a wide variety of exciting applications, although significant aspects still need further exploration, such as increasing the operational bandwidth, and enhancing experimental practicality.

Acknowledgments

This research is supported by the National Science Foundation – Civil, Mechanical and Manufacturing Innovation (NSF-CMMI) (Grant no. 1120795), and the Gordon and Betty Moore Foundation.